Quasi-Solid-State "Water-in-Swelling-Clay" Electrolytes Enabling Ultrastable Aqueous Zinc-Ion Batteries

Siyu Tian[a], Taesoon Hwang[b], Sina Malakpour Estalaki[c], Yafen Tian[d], Long Zhou[a], Tye Milazzo[c], Seunghyun Moon[c], Shiwen Wu[a], Ruda Jian[a], Kenneth Jr Balkus[c], Tengfei Luo[d,*], Kyeongjae Cho[b,*], Guoping Xiong[a,*]

[a] Department of Mechanical Engineering, The University of Texas at Dallas, 800 W Campbell Rd, Richardson, TX 75080, United States

[b] Department of Material Science Engineering, The University of Texas at Dallas, 800 W Campbell Rd, Richardson, TX 75080, United States

[c] Aerospace and Mechanical Engineering, University of Notre Dame, Notre Dame, Indiana 46556, United States

[d] Department of Chemistry & Biochemistry, The University of Texas at Dallas, 800 W Campbell Rd, Richardson, TX 75080, United States

*** Corresponding Authors**

E-mail: guoping.xiong@utdallas.edu (Guoping Xiong), kjcho@utdallas.edu (Kyeongjae Cho), tluo@nd.edu (Tengfei Luo)

Abstract:

The poor reversibility of Zn metal anodes arising from water-induced parasitic reactions poses a significant challenge to the practical applications of aqueous zinc-ion batteries (AZIBs). Herein, a novel quasi-solid-state "water-in-swelling-clay" electrolyte (WiSCE) containing zinc sulfate and swelling clay – bentonite (BT) is designed to enable highly reversible Zn metal anodes. AZIB full

cells based on the WiSCE exhibit excellent cyclic stability at various current densities, long shelf life, low self-discharge rate, and outstanding high-temperature adaptability. Particularly, the capacity of WiSCE-based AZIB full cells retains 90.47% after 200 cycles at 0.1 A/g, 96.64% after 2000 cycles at 1 A/g, and 88.29% after 5000 cycles at 3 A/g. Detailed density functional theory calculations show that strong hydrogen-bonds are formed between BT and water molecules in the WiSCE. Thus, water molecules are strongly confined by BT particularly within the interlayers, which significantly inhibits water-induced side reactions and thus greatly improves cyclic stability. Compared to the state-of-the-art "water-in-salt" electrolyte, the WiSCE can provide a significantly higher capacity at the full-cell level with a substantially reduced cost, which is promising for the design of next-generation high-performance AZIBs. This work provides a new direction for developing cost-competitive AZIBs as alternatives in grid-scale energy storage.

Keywords: Bentonite clay, Quasi-solid-state, Electrolyte additives, Zn metal anodes, Aqueous zinc-ion batteries

1. Introduction

Aqueous zinc-ion batteries (AZIBs) have attracted tremendous research interest for grid-scale energy storage applications because of their advantages such as low safety risks, abundant elemental resources, low cost, and eco-friendliness [1, 2]. Although the electrochemical performance of AZIBs has been improved over the past few years, significant challenges impeding their practical use remain due to the ubiquitous water-induced issues at the Zn/electrolyte interface such as water decompositions (e.g., hydrogen evolution reaction – HER), zinc corrosion, byproduct passivation, and dendrite growth [3, 4]. These issues can cause fast performance degradation, rapid self-discharge, and quick catastrophic failure of AZIBs during charge/discharge. Furthermore, Zn metal anodes continuously react with water over long-term resting, leading to the unsatisfactory shelf life of AZIBs [5]. At elevated temperatures, water-induced parasitic reactions become more severe owing to accelerated chemical reactions [5, 6], which further hinders the widespread applications of AZIBs.

To date, many strategies have been proposed to address water-induced challenges, including Zn surface modification [7-9], Zn crystallography modulation [10-12], separator functionalization [13-15], and electrolyte engineering [16-18]. Among them, electrolyte engineering has been widely considered the most promising strategy to regulate water activities to promote reversible Zn-metal battery chemistries in aqueous environments [19]. As summarized in Table S1, a wide range of additives have been added to baseline electrolytes (e.g., 1 – 3 M $ZnSO_4$ in water), including inorganic oxides [20-23], salts [24-27], polymers [28-30], graphene quantum dots [31] and organic compounds [32-35]. However, grid-scale energy storage devices mainly operate at current rates (C-rates, 1 C means that a battery can be fully charged or discharged in an hour) lower than 0.5 C with peak rates up to 10 C (i.e., 6 min per charge or discharge) [36, 37]. Unfortunately,

the majority of electrolyte additives (Table S1) have limited effect in enhancing the cyclic stability of AZIBs at low C-rates (≤ 10 C) or low current densities (≤ 1 A/g). This is because a high cycle number but a short run time of AZIBs achieved at high C-rates can tremendously underrate the irreversibility of time-dependent, water-induced parasitic reactions, such as HER and Zn corrosion, which has been elaborated in several reviews [37-39]. Moreover, the high cost and limited material availability of conventional additives adversely affect the advantages of AZIBs as economic and scalable alternatives. Therefore, finding low-cost and high-availability electrolyte additives that can simultaneously improve the long-term stability of AZIBs remains a daunting task for their practical applications in grid-scale energy storage.

Herein, a low-cost, quasi-solid-state "water-in-swelling-clay" electrolyte (WiSCE) was designed to provide a favorable aqueous environment for highly reversible Zn metal anodes. The WiSCE was prepared by mixing a high concentration (50% weight/volume, w/v) of swelling clay – bentonite (BT, $Al_2H_2O_{12}Si_4$) with the baseline electrolyte (BE, 2 M $ZnSO_4$ in water). The resulting WiSCE – possessed low salt concentration (1.2 M), high ionic conductivity (16.8 mS/cm), and increased storage modulus (1.1 MPa). Furthermore, water molecules could be effectively confined between the interlayers of BT crystals, leading to significantly suppressed water activities toward Zn metal anodes and thus highly reversible Zn plating/stripping in the WiSCE. In addition, the WiSCE-based AZIB full cells exhibited high Coulombic efficiency (> 99.9%), long shelf life (> 60 days), ultralow self-discharge rate (1.89 mV/day), outstanding high-temperature adaptability (50°C), and excellent cyclic stability at low and high C-rates. This work provides a new design of a cost-competitive aqueous electrolyte to design safe, durable, and reliable AZIBs. Moreover, this work opens up a new path for designing high-performance aqueous electrolytes based on swelling clays.

2. Results and discussion

2.1. Electrolyte design principles

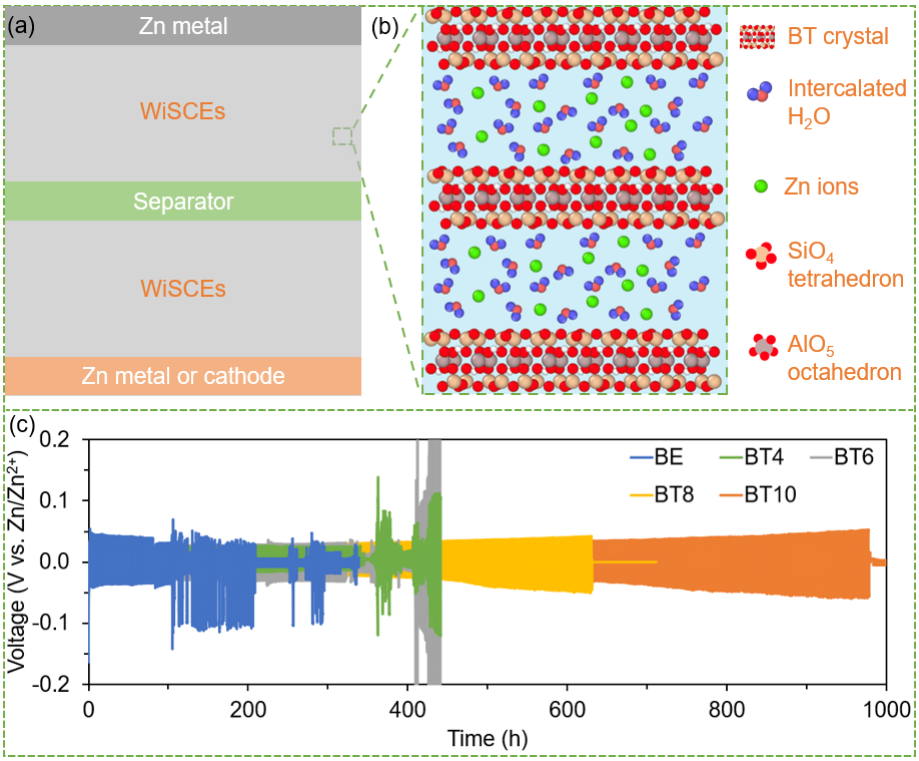

Figure 1. Schematical illustration of (a) configuration of WiSCE-based cells and (b) hydration swelling of BT. (c) Cyclic stability of Zn||Zn symmetric cells based on WiSCEs with different BT contents at a current density of 1 mA/cm^2 and an areal capacity of 1 mAh/cm^2.

Figure 1a schematically illustrates the configuration of WiSCE-based symmetric and full cells, in which an equal amount of WiSCE was uniformly pasted on each surface of the two electrodes (e.g., Zn metal anode or cathode). BT, or the synonym of montmorillonite, has two silica tetrahedral sheets (SiO_4) and a sandwiched alumina octahedral (AlO_5) sheet with extraordinary hydration swelling capability [40]. Once immersed into aqueous electrolytes, a significant amount of water molecules could be intercalated into BT crystals (Figure 1b), a phenomenon known as interlayer swelling [41-43]. We hypothesize that water activities can be remarkably suppressed by

confining water molecules within the interlayers of such mineral clays with excellent swelling capabilities, preventing Zn metal anodes from water-induced parasitic reactions and thus enhancing their reversibility in aqueous environments.

As a proof-of-concept, Zn||Zn symmetric cells based on the WiSCEs with different BT contents were assembled and cycled at 1 mA/cm^2 and 1 mAh/cm^2 (Figure 1c). The WiSCEs were denoted as BT*x*, where *x* represents the mass of BT per 10 mL of BE. For instance, the WiSCEs with 4 and 10 g of BT in 10 mL of BE were denoted as BT4 and BT10, respectively. The results showed that the cycle life of Zn||Zn symmetric cells increased with increasing BT content since more water molecules could be effectively confined by BT. Notably, the BT10-based symmetric cell displayed the longest cycle life of 980 h. In sharp contrast, the BE-based symmetric cell sustained less than 80 h with a sudden drop in voltage hysteresis. The cyclic stability of WiSCE-based AZIB full cells exhibited the same trend when varying the concentrations of BT, and the BT10-based battery displayed the highest stability during long-term cycling (Figure S1). Most importantly, other natural clays or inorganic materials without interlayer swelling capabilities but with similar chemical compositions such as kaolinite (KL, $Al_2H_4O_9Si_2$) and silicon dioxide (SiO_2) could not enhance the cyclic stability of full cells when added into BE as comparisons (Figure S2 and Figure S3). For KL or SiO_2, water molecules can only be absorbed on the particle surfaces, resulting in limited confinement effect and thus poor cyclic stability of AZIB full cells. Such a comparison between BT and KL (or SiO_2) highlighted the significance of confining water molecules within the interlayers. Moreover, BT has been widely used in industry with a low cost (~ $90 per ton with freight cost) and high yield (~ 21 million metric tons in 2020) [44, 45], rendering it the most cost-competitive electrolyte additive for AZIBs to the best of our knowledge, as summarized in Table S1. For instance, the state-of-the-art "water-in-salt" electrolyte [46], 1 mol $Zn(TFSI)_2$ and 20 mol

LiTFSI in 1 kg of water, costs $6.87 million per metric ton, which is 7,438 times higher than the cost ($924 per metric ton) of the WiSCE (see detailed cost estimation in SI). Importantly, the WiSCE-based full cell exhibited a significantly higher capacity (313 mAh/g at 0.4 C) than that (100 mAh/g at 0.2 C) of the reported AZIB full cell based on the "water-in-salt" electrolyte [46].

2.2. Electrolyte properties and structures

The BT powder exhibited an irregular flake-like shape with an average particle size of less than 10 μm (Figure S4) and consisted of Si, Al, and O as confirmed by X-ray photoelectron spectroscopy (Figure S5). Upon adding high concentrations of BT into the baseline electrolyte (i.e., 2 M $ZnSO_4$ in water), the resulting WiSCEs turned into a quasi-solid-state (Figure S6) due to the formation of gel structures between BT plates [47]. Figure 2a shows the exact water contents in the WiSCEs determined by thermogravimetric analysis (TGA) tests. The BT powder contained 8% of physically adsorbed water, which rapidly evaporated before the temperature reached 100°C. In the WiSCEs, water content monotonically decreased with increasing BT concentration. Remarkably, the water content in BT10 decreased to 41.3 wt% (Figure S7), much lower than those of BE (75.3 wt%) and previously reported polymeric hydrogel electrolytes (66.3 – 88.8 wt%) [48]. Moreover, the complete loss of water in the WiSCEs was significantly delayed up to 170°C, suggesting that water molecules were strongly bounded to the BT host.

The existence of interlayer water in the WiSCEs was evidenced by X-ray diffraction (XRD) tests, as shown in Figure 2b. The BT powder showed an initial basal spacing (d_{001}) of 12.2 Å and several characteristic diffraction peaks of montmorillonite at 7°, 20°, 29°, 35° and quartz at 27° [49]. In the WiSCEs, the d_{001} of BT crystals increased to 18.9 Å because of water intercalation, corresponding to an enlarged interlayer spacing from 2.6 to 9.3 Å (Figure S8) [50]. Based on the

interlayer spacing, a volume expansion ratio (ER) of 54.9% of the swelled BT in BT10 electrolyte could be determined according to the method described in prior work [51], which suggested that approximately 35.6 vol% of free water from the BE was confined within the interlayers of BT crystals (see calculation details in SI). Additionally, water molecules could also be adsorbed on the external surface of BT [52-54], resulting in significantly decreased amounts of free water and low water activities in the WiSCEs. Moreover, the enlarged interlayer spacing not only accommodated more water molecules between BT layers but also facilitated ion transport through the nanochannels in the viscous quasi-solid-state electrolytes. Consequently, BT10 still maintained a high ionic conductivity of 16.8 mS/cm (Figure 2c) given the ultrahigh viscosity (1363.4 Pa·s) and diluted salt concentration (1.2 M, Figure S9) upon BT addition. In comparison, BE with a salt concentration of 2 M exhibited an ionic conductivity of 51.9 mS/cm and a low viscosity of 6.6 Pa·s. In the WiSCEs, the unique layered structure of BT may enable the formation of fast ion-conducting pathways, which can reduce ion diffusion length and facilitate fast ion transport [55]. The addition of BT also affected the pH of the WiSCEs because of the hydrolysis of BT and the adsorption of Zn ions [56, 57]. For the electrolytes ranging from BT4 to BT10, their pH values stabilized at approximately 5.5 (Figure S10), which could alleviate Zn corrosion and hydrogen evolutions in such near-neutral environments [25]. In terms of viscoelastic properties, BT10 electrolyte exhibited the highest storage modulus (G′) of 1.07 MPa (Figure 2d), signifying its superior mechanical resistance against Zn dendrite growth [58, 59]. Moreover, the WiSCEs exhibited solid-like rheological properties (Figure S11) due to the formation of gel structures [40, 60], which is highly desired in practical applications vulnerable to electrolyte leakage [61, 62].

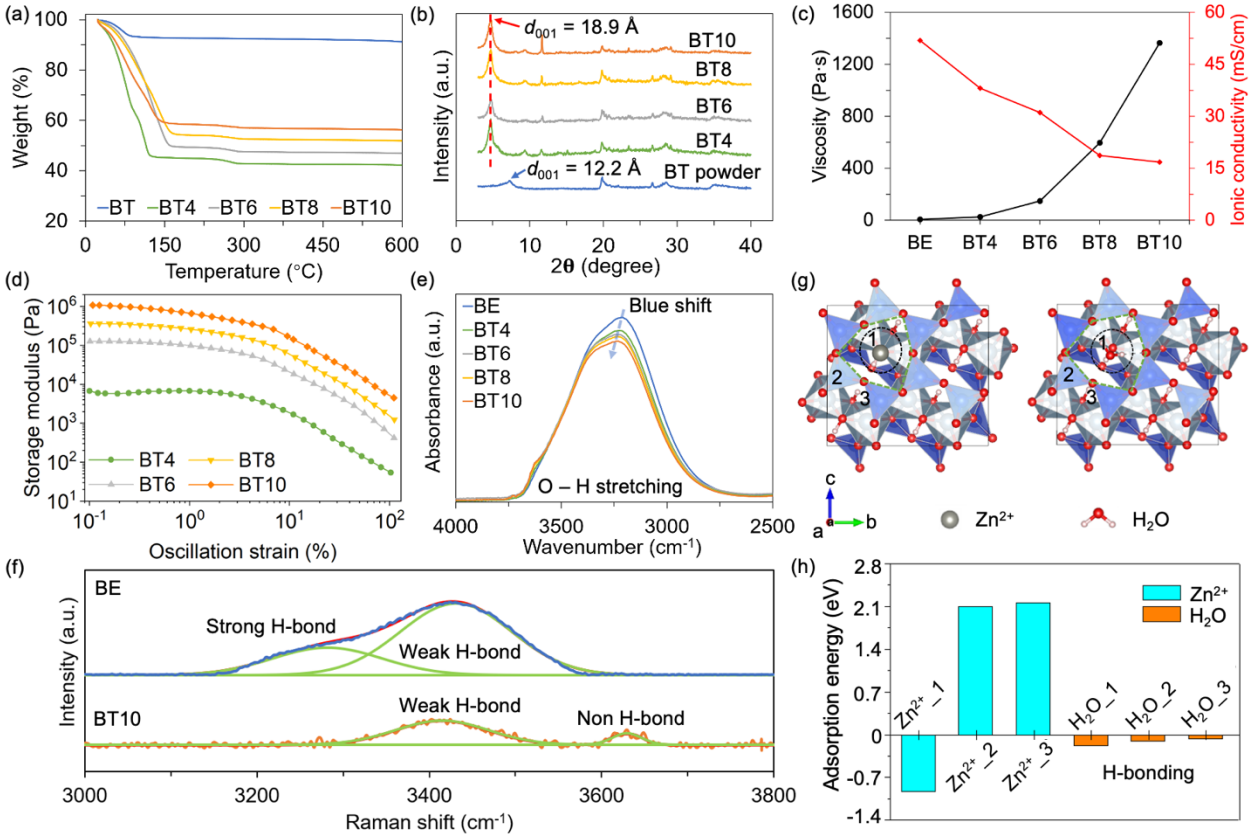

Figure 2. Physical and chemical properties of BT and WiSCEs. (a) TGA curves. (b) XRD curves. (c) Ionic conductivities and viscosities of the WiSCEs with different amounts of BT. (d) Storage modulus. (e) FTIR spectra. (f) Raman spectra. (g) Atomic surface model of Zn^{2+} and H_2O adsorption at site 1 (Zn^{2+}_1 and H_2O_1) of the BT crystal. (h) Adsorption energies of Zn^{2+} and H_2O at different sites.

To further unveil the interactions between water molecules and BT, Fourier-transform infrared (FTIR) spectroscopy and Raman spectroscopy were conducted. In the FTIR spectra (Figure 2e and Figure S12), the broad peak ranging from 2700 to 3700 cm^{-1} because of O – H stretching vibration shifted to higher wavenumbers with a steadily decreased magnitude when increasing the concentration of BT. This implied the strengthened hydrogen-bonding (H-bonding) interactions between water and BT and the weakened H-bonding interactions among water molecules [63-65]. The chemical environment of water was further investigated by Raman tests, as shown in Figure 2f. Compared with BE, the O – H stretching vibration in the Raman spectrum of BT10 electrolyte

was largely suppressed because of the limited amounts of free water molecules [66]. Moreover, in the Raman spectrum of BE, the broad peak of O – H stretching vibration can be convolved into two major peaks located at 3280 and 3430 cm^{-1} corresponding to water molecules with strong and weak H-bonds [67], respectively. In BT10 electrolyte, the H-bonds between water molecules were significantly weakened. In detail, the peak assigned to water molecules with strong H-bonds was absent, and a new peak located at 3630 cm^{-1} appeared because of non-hydrogen-bound water molecules [67]. These results suggested that the addition of BT effectively reconstructed the H-bonding networks between water molecules and resulted in low water activities in BT10 electrolyte. The stretching vibrations of SO_4^{2-} located at 454 and 623 cm^{-1} were also largely blue-shifted (Figure S13) in the presence of BT, implying the changes of solvation environments [68].

To validate the experimental results, the adsorption of H_2O and Zn^{2+} onto the surface of BT crystals was examined by density functional theory (DFT) calculations, as shown in Figure 2g. Three adsorption configurations (Figure S14 and Figure S15) were defined due to the symmetricity of the (001) basal plane of BT crystals. Figure 2h shows the adsorption energies of Zn^{2+} and H_2O at different sites. At site 1 – the center of the hexagon-like oxygen rings, Zn^{2+} adsorption was thermodynamically stable with an adsorption energy of -0.96 eV attributed to the Coulombic interactions between Zn^{2+} and oxygen atoms on BT surface. The strong Zn^{2+} adsorption of BT could potentially alter the solvation environment of Zn^{2+} and their diffusion pathways, thus facilitating fast ion diffusions and reversible Zn plating/stripping. Nevertheless, molecular dynamics simulations (Figure S16, see details in SI) indicated that the Zn ions existing within the BT interlayers or in BE possessed the same solvation structure with a coordination number of 6 (Figure S17) since the interlayer spacing (9.3 Å) of swelled BT is larger than the size (8.6 Å) of solvated zinc ions – $Zn^{2+}(H_2O)_6$ [69]. Meanwhile, stable water adsorptions were observed on the

entire BT surface with a lowest adsorption energy of -0.18 eV at site 1, suggesting the excellent hydration swelling capabilities of BT. Notably, at site 1, a strong H-bond was formed between the adsorbed H_2O and the oxygen atom on BT surface (Figure S14a). These results implied that the strong water adsorption by BT was enabled by the formation of H-bonds between the two species, which further resulted in the low water activities in the quasi-solid-state WiSCEs.

2.3. Stability of Zn metal in the WiSCEs

Figure 3a shows the comparative chronoamperometry (CA) curves of the Zn metal electrodes in BE and WiSCEs with a constant overpotential of -150 mV. In BE, the current density of the Zn metal electrode increased rapidly over 120 s, indicating a long 2D diffusion process and remarkable tipping effect induced by Zn dendrite growth [70, 71]. On the contrary, the plating of Zn in the WiSCEs quickly developed into a stable 3D diffusion process after a very short period (~ 20 s) of Zn nucleation and 2D diffusion. This result suggested the formation of a smooth and flat Zn/electrolyte interface owing to localized Zn^{2+} reduction and uniform Zn deposition in the WiSCEs [71]. The HER behavior of Zn metal electrodes in BE and BT10 electrolytes was investigated by linear sweep voltammetry (LSV) tests, as shown in Figure 3b. In BT10 electrolyte, the HER onset potential was delayed to -1.04 V vs. Ag/AgCl with a low current during hydrogen evolutions, which could be attributed to the limited free water molecules, low water activities, and near-neutral pH (~ 5.5) environment of the quasi-solid-state electrolyte. The oxygen evolution reaction (Figure S18) was also retarded and suppressed in BT10 electrolyte, suggesting the high stability of water molecules.

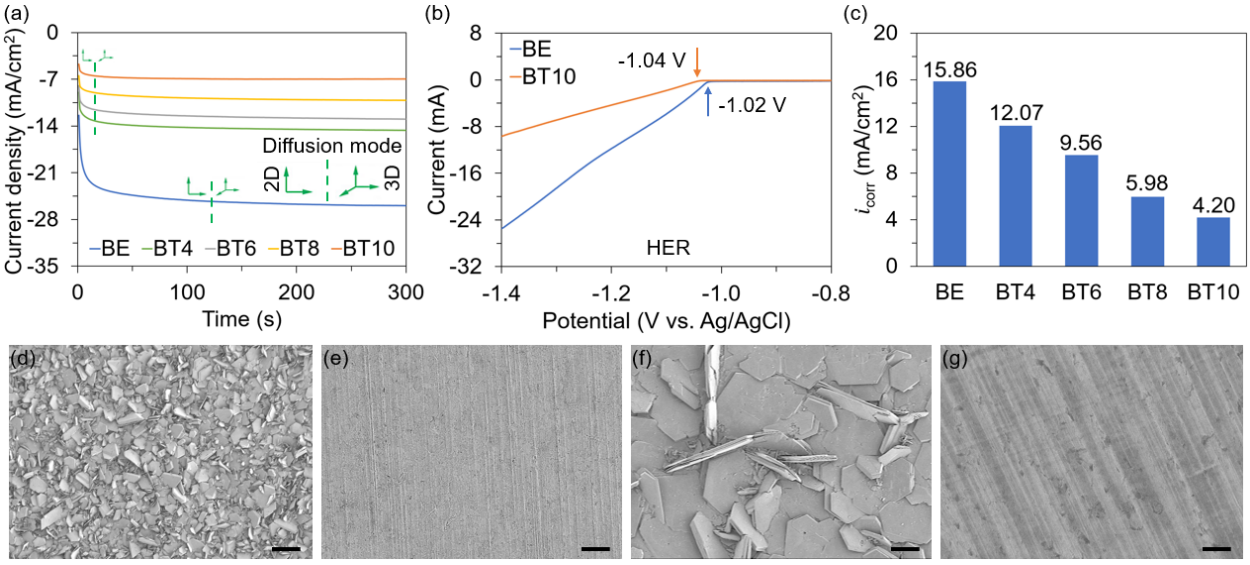

Figure 3. (a) CA curves of WiSCEs with different amounts of BT. (b) LSV curves of BE and BT10 electrolytes. (c) The corrosion current densities of Zn metal electrodes in the WiSCEs fitted from Tafel curves. SEM images of Zn metal soaked in (d) BE and (e) BT10 electrolytes for 30 days at room temperature. SEM images of Zn metal soaked in (f) BE and (g) BT10 electrolytes for 10 days at 50°C. Scale bar: (d)-(g) 50 μm.

The comparative anti-corrosion performance of Zn metal in BE and WiSCEs was investigated by Tafel and soaking tests. As shown in Figure 3c, the high corrosion current density (i_{corr} = 15.86 mA/cm^2) indicated the aggressive corrosion of Zn metal in BE. In WiSCEs, the i_{corr} monotonically decreased to 4.20 mA/cm^2 in BT10 when increasing the BT content. The Zn metal electrodes also exhibited more negative corrosion potentials (approximately -1.01 V vs. Ag/AgCl) in WiSCEs compared with that (-1.00 V vs. Ag/AgCl) in BE (Figure S19). These results reflected the low corrosion rate and excellent corrosion resistance of Zn metal in the WiSCEs due to the effective suppression of water activities. The extraordinary anti-corrosion performance of Zn metal in the highly concentrated WiSCEs was further confirmed by soaking tests. After being soaked in BE for 30 days at room temperature, the pristine smooth Zn surface (Figure S20) was passivated

by numerous flake-like byproducts (Figure 3d), indicating the severe corrosion and passivation of Zn in the mild acidic electrolyte. In contrast, the Zn metal soaked in BT10 electrolyte under the same condition remained nearly intact and free of precipitated byproducts (Figure 3e and Figure S21a). Even at an elevated temperature (50°C), Zn metal still demonstrated superior corrosion resistance in BT10 electrolyte. Unlike the intense passivation of Zn surface by the precipitation of large-flake byproducts in BE (Figure 3f), the Zn surface remained nearly free of byproducts (Figure 3g and Figure S21b) after being soaked in BT10 electrolyte for 10 days at 50°C, which was further evidenced by XRD tests (Figure S22). Moreover, the rate of hydrogen evolutions during the soaking test was quantified using an analytical balance (see details in SI). As shown in Figure S23, the hydrogen generation rate reached 28 μmol/(h·cm^2) or 0.68 mL/(h·cm^2) in BE while no hydrogen evolutions were observed in BT10 electrolyte.

2.4. Reversibility of Zn metal anodes in WiSCEs

Zn||Zn and Cu||Zn cells were assembled to investigate the reversibility of Zn metal anodes in the WiSCEs. Figure 4a compares the cyclic stability of Zn||Zn symmetric cells based on BE and BT10 electrolytes at a current density of 1 mA/cm^2 and a capacity of 1 mAh/cm^2. A typical BE-based Zn||Zn symmetric cell failed after approximately 80 h with significant voltage fluctuations. During long-term cycling, abundant byproducts and porous Zn deposits were formed on the surface of Zn metal anodes (Figure S24a-b), which resulted in a short cycle life of the BE-based symmetric cell. However, in BT10 electrolyte, the cycled Zn metal anode exhibited a dendrite-free morphology (Figure S24c-d) because of the significantly suppressed hydrogen evolutions, Zn corrosion, and dendrite growth. Therefore, the cycle life of the BT10-based Zn||Zn symmetric cell can be prolonged to 980 h with lower voltage hysteresis (Figure S25). Nevertheless, the voltage hysteresis gradually increased during cycling because a small amount of byproducts was still

produced on the surface of Zn metal anode, as confirmed by SEM (Figure S24c) and XRD (Figure S26), which remains to be optimized in future work. As shown in Figure S27, BT10-based Zn||Zn symmetric cell also exhibited a lower charge transfer resistance of 230 Ω compared with that (270 Ω) of the BE-based Zn||Zn cell, implying its fast kinetics during Zn plating/stripping.

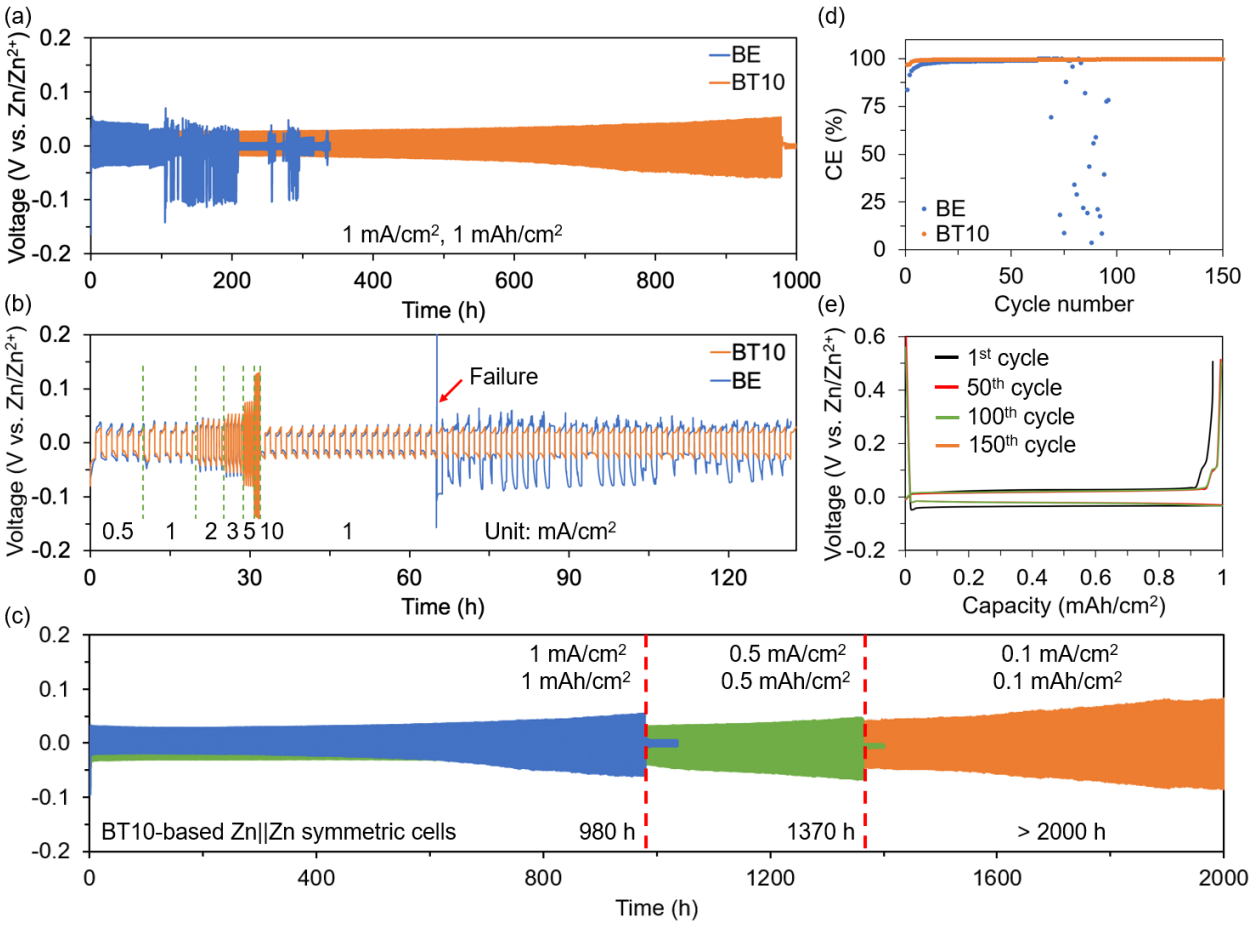

Figure 4. (a) Cyclic stability of Zn||Zn symmetric cells in BE and BT10 electrolytes at a current density of 1 mA/cm^2 and a capacity of 1 mAh/cm^2. (b) Rate capability of Zn||Zn symmetric cells in BE and BT10 electrolytes. (c) Cyclic stability of Zn||Zn symmetric cells in BE and BT10 electrolytes at different current densities and areal capacities. (d) Coulombic efficiencies and (e) voltage profiles of Cu||Zn half cells in BE and BT10 electrolytes at a current density of 1 mA/cm^2.

Figure 4b shows the rate capabilities of the Zn||Zn symmetric cells based on BE and BT10 electrolytes. The BT10-based symmetric cell exhibited a stable voltage profile with low voltage

hysteresis upon changing current densities. Comparatively, the BE-based symmetric cell quickly failed when switching the current density from 10 to 1 mA/cm^2. As shown in Figure 4c, when cycled at lower areal capacities of 0.5 and 0.1 mAh/cm^2 with a C-rate of 1 C, the cycle life of the BT10-based symmetric cells could be further extended to 1370 h and 2000 h, respectively. The enhanced Zn plating/stripping reversibility could be mainly attributed to the low water activities and high mechanical stiffness of the quasi-solid-state BT10 electrolyte, making it effective in suppressing HER, Zn corrosion, and dendrite growth over long-term cycling. Meanwhile, the quasi-solid-state BT10 electrolyte significantly inhibited water-induced parasitic reactions that would otherwise result in low Coulombic efficiency (CE) during Zn plating/stripping. As shown in Figure 4d, the BE-based Cu||Zn half cell possessed a low initial CE of 83.75% and failed after 60 cycles at 1 mA/cm^2 with a significant drop of voltage hysteresis (Figure S28). In comparison, the initial CE of the BT10-based Cu||Zn half cell increased to 96.87%, and a high average CE of 99.53% was achieved during the cycling. The corresponding voltage profiles shown in Figure 4e remained unchanged from 50 to 150 cycles, confirming remarkably inhibited water-induced parasitic reactions in the quasi-solid-state BT10 electrolyte. Furthermore, the nucleation overpotential dropped dramatically from 41 to 12 mV (Figure S29), suggesting a lower energy barrier of Zn reduction in BT10 electrolyte, which is conducive to the uniform nucleation and deposition of Zn metal [34].

2.5. Electrochemical performance of the WiSCE-based full cells

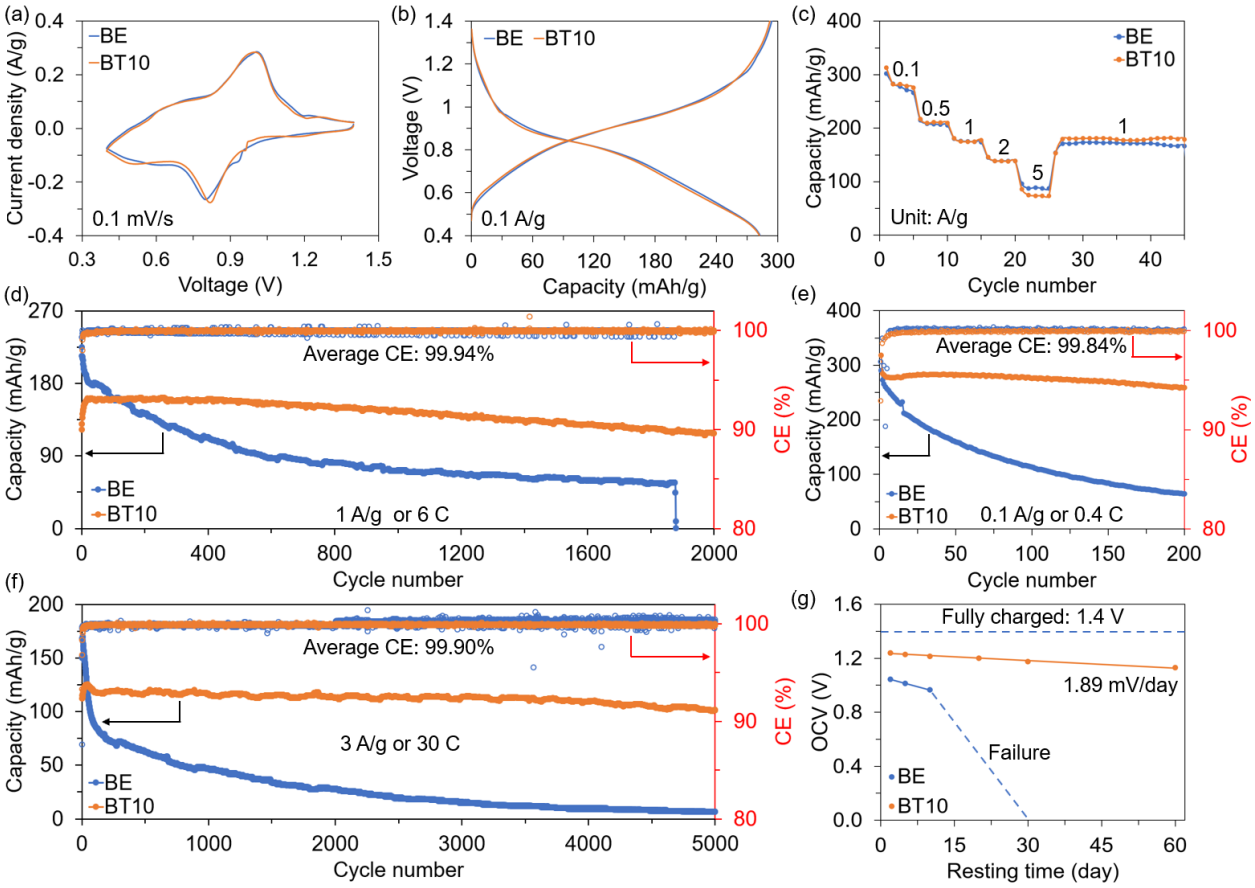

Figure 5. The electrochemical performance of Zn||NVO full cells based on BE and BT10 electrolytes. (a) CV curves at a scan rate of 0.1 mV/s. (b) Galvanostatic charge/discharge curves at a current density of 0.1 A/g. (c) Rate capabilities. Long-term cyclic stability of Zn||NVO full cells based on BE and BT10 electrolytes at different current densities of (d) 1 A/g, (e) 0.1 A/g, and (f) 3 A/g. (g) Self-discharge performance of fully charged Zn||NVO full cells based on BE and BT10 electrolytes.

To demonstrate the advantages of the WiSCEs in practical applications, AZIB full cells were assembled using the widely reported cathode material – sodium doped V_2O_5 (NVO) [72, 73]. Figure 5a and Figure 5b show the cyclic voltammetry (CV) and galvanostatic charge/discharge curves of the Zn||NVO full cells based on BE and BT10 electrolytes, respectively. Similar redox peaks during the CV test and nearly identical voltage profiles during charge/discharge were

observed, suggesting that no extra redox or parasitic reactions were introduced by BT. Figure 5c shows the rate capabilities of the full cells based on the two electrolytes, in which the BT10-based cell exhibited discharge capacities of 313.0, 217.2, 181.2, 146.1, 86.1 mAh/g at current densities of 0.1, 0.5, 1, 2, 5 A/g, respectively. The specific capacity of the BT10-based full cell recovered to 180.1 mAh/g when the current density returned to 1 A/g, higher than that (170.8 mAh/g) of the BE-based cell. Moreover, the BT10-based full cell exhibited a lower charge transfer resistance compared with that of the BE-based cell (Figure S30), consistent with the results obtained in symmetric cells.

Figures 5d-f show the comparative long-term cyclic stability and CEs of the Zn||NVO full cells based on BE and BT10 electrolytes at three different current densities. At a current density of 1 A/g, the BT10-based full cell exhibited an initial discharge capacity of 122.1 mAh/g and maintained a discharge capacity of 118.0 mAh/g after 2000 cycles (Figure 5d), corresponding to an ultrahigh capacity retention rate of 96.64%. In contrast, the capacity of the BE-based full cell retained only 32.01% after 1000 cycles and failed after approximately 1900 cycles. At a lower current density of 0.1 A/g, the BT10-based full cell displayed a high initial discharge capacity of 318.5 mAh/g, as shown in Figure 5e. The capacity decreased to 284.5 mAh/g at the 2^{nd} cycle and retained 257.4 mAh/g at the 200^{th} cycle, corresponding to a high retention rate of 90.47% over 200 cycles, while the BE-based full cell only retained 21.49% of its initial capacity after 200 cycles at 0.1 A/g due to the severe parasitic reactions. At a high current density of 3 A/g, the capacity of the BT10-based full cell retained 88.29% after 5000 cycles, substantially outperforming that (4.44%) of the BE-based full cell under the same condition (Figure 5f). Moreover, the CEs of the BT10-based full cells were much more stable than those of BE-based batteries at the three current densities. Compared with previously reported AZIBs with different electrolyte additives, the

BT10-based full cells exhibited substantially better cyclic stability at practical C-rates (Table S1). To understand the remarkably improved cyclic stability of BT10-based full cells, the morphology of the cycled Zn metal anode was characterized by SEM (Figure S31). After 1000 cycles at 3 A/g, the Zn metal anode cycled in BT10 electrolyte maintained a dendrite-free morphology due to the high stiffness of the quasi-solid-state electrolyte and suppressed water activities, which is in sharp contrast with that of the Zn metal anode cycled in BE. These results confirmed that BT, a low-cost and high-availability electrolyte additive, provided a favorable aqueous environment for Zn metal anodes. Thus, the cyclability of BT10-based full cells could be significantly enhanced at low and high charge/discharge C-rates, which is highly desired in practical grid-scale energy storage applications.

In addition, Figure 5g exhibits the comparative self-discharge performance of the Zn||NVO full cells based on BE and BT10 electrolytes, which is evaluated by monitoring the open circuit voltage (OCV) of fully charged cells during rest time up to 60 days before being fully discharged to 0.4 V. Figure S32 shows the corresponding voltage profiles of the Zn||NVO full cells during resting. Because of the severe parasitic reactions, the OCV of the BE-based full cells quickly dropped to 1.04 V after resting for 2 days and retained only 0.96 V after resting for 10 days. When further extending the resting time, drastic voltage drops were observed for the BE-based full cells, indicating the failure of these batteries because of severe hydrogen evolutions and Zn corrosion during long-term resting. On the contrary, for the BT10-based full cells, the OCV dropped to 1.24 V after resting for 2 days and retained 1.13 V after resting for 60 days, corresponding to an ultralow voltage degradation rate of 1.89 mV/day or 0.079 mV/h, which is one order of magnitude lower than those of previously reported aqueous batteries [74, 75]. Moreover, the BT10-based full cell still retained 43.74% of its charge capacity after resting for 60 days (Figure S33), demonstrating

that the quasi-solid-state electrolyte is highly promising for practical AZIBs that require long-term storage capabilities.

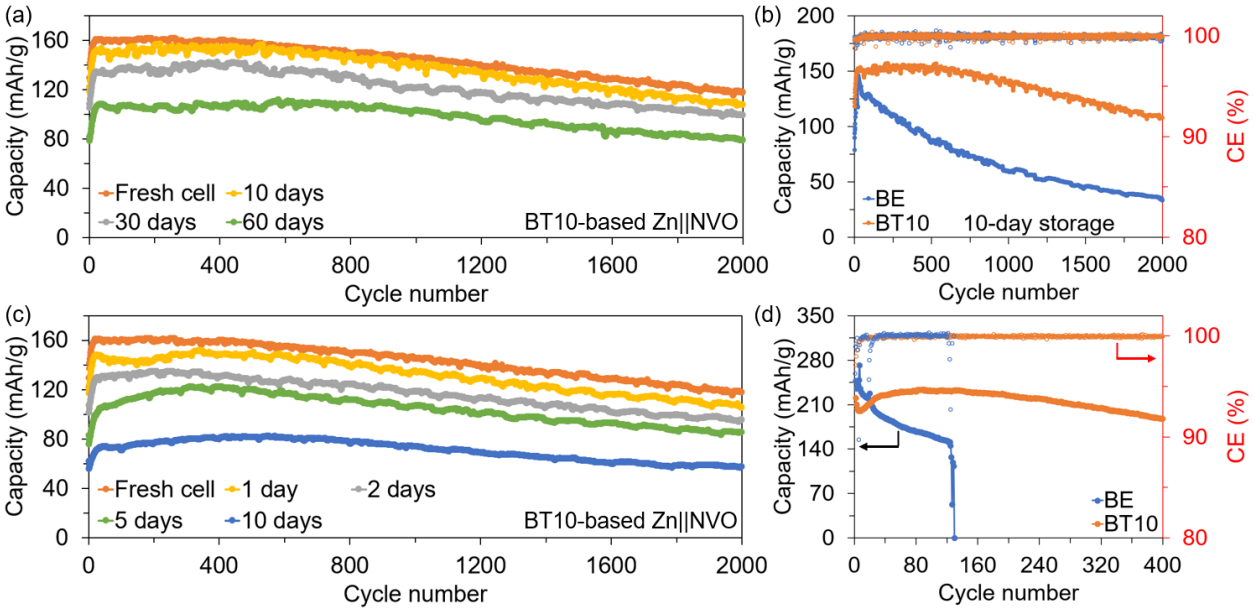

Figure 6. (a) Cyclic stability of BT10-based full cells after being stored at room temperature for up to 60 days. (b) Cyclic stability of BE- and BT10-based full cells after 10-day storage at room temperature. (c) Cyclic stability of BT10-based full cells after storage at 50°C for up to 10 days. (d) Cyclic stability of BT10-based full cells working at 50°C at a current density of 1 A/g.

The superior long-term-storage capability of the BT10-based full cells was further demonstrated by storing the assembled full cells at room temperature for up to 60 days before cyclic galvanostatic charge/discharge tests. As shown in Figure 6a, after 60 days of storage, the BT10-based full cell still featured extraordinary cyclic stability and high average CE (99.94%, Figure S34) over 2000 cycles at 1 A/g, indicating its ultralong shelf life and outstanding resistance to performance degradation during long-term storage. In comparison, Figure 6b exhibits that the BE-based full cell suffered from severe capacity degradation after 10-day storage and failed when further extending the storage time (Figure S35). At a higher temperature of 50°C, the shelf life of the BE-

based full cell was further decreased to less than 1 day (Figure S36) due to the significantly accelerated hydrogen evolutions and Zn corrosion. However, as shown in Figure 6c, the BT10-based full cell still exhibited excellent cyclic stability over 2000 cycles at 1 A/g after 10-day storage at 50°C, signifying its long shelf life at elevated temperatures. Moreover, Figure 6d shows that the as-assembled BT10-based full cell could safely operate at 50°C over 400 cycles at 1 A/g and retained 84.54% of its initial capacity of 220.5 mAh/g, outperforming the high-temperature adaptability of most AZIBs reported in prior work (Table S2). These results manifested the extraordinary shelf life and high-temperature adaptability of the BT10-based full cells toward practical energy storage applications.

3. Conclusions

A new type of quasi-solid-state WiSCE was developed to reduce free water contents and suppress water activities for highly reversible Zn plating/stripping in aqueous environments. By introducing a low-cost and high-availability swelling clay – BT, into the mild acidic electrolyte, water molecules could be strongly confined within the interlayers of BT crystals, leading to low water activities in the quasi-solid-state electrolyte. The formation of gel structures between BT plates also enabled the high stiffness and high viscosity of the BT-based electrolyte. Therefore, the dendrite growth, Zn corrosion, and gas evolutions at the Zn/electrolyte interface could be effectively inhibited. In addition, the WiSCE-based Zn||NVO full cells exhibited ultrahigh cyclic stability at low and high current densities. Particularly, the capacities of the full cells retained 90.47% after 200 cycles at 0.1 A/g, 96.64% after 2000 cycles at 1 A/g, and 88.29% after 5000 cycles at 3 A/g. This work revealed that a natural swelling clay – BT with layered structures could effectively enhance the cyclic stability, safety, and durability of AZIBs. Benefiting from the low cost, high availability, and facile functionalization of BT, the WiSCE would be promising to design high-

performance AZIBs and accelerate their commercialization in grid-scale energy storage applications.

Supplementary Information

Supplementary data associated with this article is available online or from the author.

Acknowledgments

G.X. thanks the University of Texas at Dallas startup fund and the support from the NSF (Grant No. CBET-1937949 and CBET-1949962). T.L. thanks the support from the NSF (Grant No. CBET-1937923 and CBET-1949910) for support.

Declaration of Competing Interest

The authors declare that they have no known competing financial interests or personal relationships that could have appeared to influence the work reported in this paper.

Data Availability Statement

The data that support the findings of this study are available from the corresponding author upon reasonable request.

References

1. D Chao, W Zhou, F Xie, C Ye, H Li, M Jaroniec, and S-Z Qiao, Roadmap for advanced aqueous batteries: From design of materials to applications. *Science Advances*. **6**(21): p. eaba4098.
2. N Guo, W Huo, X Dong, Z Sun, Y Lu, X Wu, L Dai, L Wang, H Lin, H Liu, H Liang, Z He, and Q Zhang, A review on 3D zinc anodes for zinc ion batteries. *Small Methods*, 2022. **6**(9): p. 2200597.

3. W Du, EH Ang, Y Yang, Y Zhang, M Ye, and CC Li, Challenges in the material and structural design of zinc anode towards high-performance aqueous zinc-ion batteries. *Energy & Environmental Science*, 2020. **13**(10): p. 3330-3360.
4. W Guo, Z Cong, Z Guo, C Chang, X Liang, Y Liu, W Hu, and X Pu, Dendrite-free Zn anode with dual channel 3D porous frameworks for rechargeable Zn batteries. *Energy Storage Materials*, 2020. **30**: p. 104-112.
5. Z Chen, X Li, D Wang, Q Yang, L Ma, Z Huang, G Liang, A Chen, Y Guo, B Dong, X Huang, C Yang, and C Zhi, Grafted MXene/polymer electrolyte for high performance solid zinc batteries with enhanced shelf life at low/high temperatures. *Energy & Environmental Science*, 2021. **14**(6): p. 3492-3501.
6. C Xie, Y Li, Q Wang, D Sun, Y Tang, and H Wang, Issues and solutions toward zinc anode in aqueous zinc-ion batteries: A mini review. *Carbon Energy*, 2020. **2**(4): p. 540-560.
7. L Hong, L-Y Wang, Y Wang, X Wu, W Huang, Y Zhou, K-X Wang, and J-S Chen, Toward hydrogen-free and dendrite-free aqueous zinc batteries: Formation of zincophilic protective layer on Zn anodes. *Advanced Science*, 2022. **9**(6): p. 2104866.
8. C Deng, X Xie, J Han, Y Tang, J Gao, C Liu, X Shi, J Zhou, and S Liang, A sieve-functional and uniform-porous kaolin layer toward stable zinc metal anode. *Advanced Functional Materials*, 2020. **30**(21): p. 2000599.
9. X Liu, F Yang, W Xu, Y Zeng, J He, and X Lu, Zeolitic imidazolate frameworks as Zn^{2+} modulation layers to enable dendrite-free Zn anodes. *Advanced Science*, 2020. **7**(21): p. 2002173.
10. Z Chen, J Zhao, Q He, M Li, S Feng, Y Wang, D Yuan, J Chen, HN Alshareef, and Y Ma, Texture control of commercial Zn foils prolongs their reversibility as aqueous battery anodes. *ACS Energy Letters*, 2022. **7**(10): p. 3564-3571.
11. SD Pu, C Gong, YT Tang, Z Ning, J Liu, S Zhang, Y Yuan, D Melvin, S Yang, L Pi, J-J Marie, B Hu, M Jenkins, Z Li, B Liu, SCE Tsang, TJ Marrow, RC Reed, X Gao, PG Bruce, and AW Robertson, Achieving ultrahigh-rate planar and dendrite-free zinc electroplating for aqueous zinc battery anodes. *Advanced Materials*, 2022. **34**(28): p. 2202552.
12. Z Yi, J Liu, S Tan, Z Sang, J Mao, L Yin, X Liu, L Wang, F Hou, SX Dou, H-M Cheng, and J Liang, An ultrahigh rate and stable zinc anode by facet-matching-induced dendrite regulation. *Advanced Materials*, 2022. **34**(37): p. 2203835.
13. Y Yang, T Chen, M Zhu, G Gao, Y Wang, Q Nie, Y Jiang, T Xiong, WSV Lee, and J Xue, Regulating dendrite-free Zn deposition by a self-assembled OH-terminated SiO_2 nanosphere layer toward a Zn metal anode. *ACS Applied Materials & Interfaces*, 2022. **14**(33): p. 37759-37770.
14. Y Guo, W Cai, Y Lin, Y Zhang, S Luo, K Huang, H Wu, and Y Zhang, An ion redistributor enabled by cost-effective weighing paper interlayer for dendrite free aqueous zinc-ion battery. *Energy Storage Materials*, 2022. **50**: p. 580-588.
15. J Cao, D Zhang, C Gu, X Wang, S Wang, X Zhang, J Qin, and Z-S Wu, Manipulating crystallographic orientation of zinc deposition for dendrite-free zinc ion batteries. *Advanced Energy Materials*, 2021. **11**(29): p. 2101299.
16. R Meng, H Li, Z Lu, C Zhang, Z Wang, Y Liu, W Wang, G Ling, F Kang, and Q-H Yang, Tuning Zn-ion solvation chemistry with chelating ligands toward stable aqueous Zn anodes. *Advanced Materials*, 2022. **34**(37): p. 2200677.

17. Y Lv, M Zhao, Y Du, Y Kang, Y Xiao, and S Chen, Engineering a self-adaptive electric double layer on both electrodes for high-performance zinc metal batteries. *Energy & Environmental Science*, 2022. **15**(11): p. 4748-4760.
18. H Qin, W Kuang, N Hu, X Zhong, D Huang, F Shen, Z Wei, Y Huang, J Xu, and H He, Building metal-molecule interface towards stable and reversible Zn metal anodes for aqueous rechargeable zinc batteries. *Advanced Functional Materials*, 2022. **32**(47): p. 2206695.
19. YS Meng, V Srinivasan, and K Xu, Designing better electrolytes. *Science*. **378**(6624): p. eabq3750.
20. J Zhou, L Zhang, M Peng, X Zhou, Y Cao, J Liu, X Shen, C Yan, and T Qian, Diminishing interfacial turbulence by colloid-polymer electrolyte to stabilize zinc ion flux for deep-cycling Zn metal batteries. *Advanced Materials*, 2022. **34**(21): p. 2200131.
21. J Gao, X Xie, S Liang, B Lu, and J Zhou, Inorganic colloidal electrolyte for highly robust zinc-ion batteries. *Nano-Micro Letters*, 2021. **13**(1): p. 69.
22. C Li, X Xie, H Liu, P Wang, C Deng, B Lu, J Zhou, and S Liang, Integrated 'all-in-one' strategy to stabilize zinc anodes for high-performance zinc-ion batteries. *National Science Review*, 2022. **9**(3): p. nwab177.
23. J Cao, D Zhang, Y Yue, R Chanajaree, S Wang, J Han, X Zhang, J Qin, and Y Huang, Regulating solvation structure to stabilize zinc anode by fastening the free water molecules with an inorganic colloidal electrolyte. *Nano Energy*, 2022. **93**: p. 106839.
24. W Zhang, Y Dai, R Chen, Z Xu, J Li, W Zong, H Li, Z Li, Z Zhang, J Zhu, F Guo, X Gao, Z Du, J Chen, T Wang, G He, and IP Parkin, Highly reversible zinc metal anode in a dilute aqueous electrolyte enabled by a pH buffer additive. *Angewandte Chemie International Edition*, 2022. **n/a**(n/a): p. e202212695.
25. D Han, Z Wang, H Lu, H Li, C Cui, Z Zhang, R Sun, C Geng, Q Liang, X Guo, Y Mo, X Zhi, F Kang, Z Weng, and Q-H Yang, A Self-Regulated Interface toward Highly Reversible Aqueous Zinc Batteries. *Advanced Energy Materials*, 2022. **12**(9): p. 2102982.
26. Q Zhang, Y Ma, Y Lu, Y Ni, L Lin, Z Hao, Z Yan, Q Zhao, and J Chen, Halogenated Zn^{2+} solvation structure for reversible Zn metal batteries. *Journal of the American Chemical Society*, 2022. **144**(40): p. 18435-18443.
27. Z Hu, F Zhang, Y Zhao, H Wang, Y Huang, F Wu, R Chen, and L Li, A self-regulated electrostatic shielding layer toward dendrite-free Zn batteries. *Advanced Materials*, 2022. **34**(37): p. 2203104.
28. J Zhou, M Peng, X Xia, S Qian, Z Wang, C Zhu, X Zeng, H Ji, S Wang, X Zhou, J Liu, X Shen, Y Cheng, T Qian, and C Yan, New type of dynamically "solid–liquid" interconvertible electrolyte for high-rate Zn metal battery. *Nano Letters*, 2022. **22**(7): p. 2898-2906.
29. S Gao, J Han, Z Liu, K Wang, K Jiang, C Guo, Y Tan, D Zhou, and W Shi, Polyvinyl pyrrolidone as electrolyte additive for aqueous zinc batteries with MnO_2 cathode. *Journal of The Electrochemical Society*, 2021. **168**(8): p. 080514.
30. N Wang, Y Yang, X Qiu, X Dong, Y Wang, and Y Xia, Stabilized rechargeable aqueous zinc batteries using ethylene glycol as water blocker. *ChemSusChem*, 2020. **13**(20): p. 5556-5564.
31. H Zhang, R Guo, S Li, C Liu, H Li, G Zou, J Hu, H Hou, and X Ji, Graphene quantum dots enable dendrite-free zinc ion battery. *Nano Energy*, 2022. **92**: p. 106752.

32. W Xu, K Zhao, W Huo, Y Wang, G Yao, X Gu, H Cheng, L Mai, C Hu, and X Wang, Diethyl ether as self-healing electrolyte additive enabled long-life rechargeable aqueous zinc ion batteries. *Nano Energy*, 2019. **62**: p. 275-281.
33. H Zhang, Y Zhong, J Li, Y Liao, J Zeng, Y Shen, L Yuan, Z Li, and Y Huang, Inducing the preferential growth of Zn (002) plane for long cycle aqueous Zn-ion batteries. *Advanced Energy Materials*, 2022. **n/a**(n/a): p. 2203254.
34. Y Zhong, Z Cheng, H Zhang, J Li, D Liu, Y Liao, J Meng, Y Shen, and Y Huang, Monosodium glutamate, an effective electrolyte additive to enhance cycling performance of Zn anode in aqueous battery. *Nano Energy*, 2022. **98**: p. 107220.
35. LM Peng Sun, Wanhai Zhou, Meijia Qiu, Zilong Wang, Dongliang Chao, Wenjie Mai, Simultaneous regulation on solvation shell and electrode interface for dendrite-free Zn ion batteries achieved by a low-cost glucose additive. *Angewandte Chemie*, 2021. **133**(33): p. 18395-18403.
36. HC Hesse, M Schimpe, D Kucevic, and A Jossen *Lithium-ion battery storage for the grid—A review of stationary battery storage system design tailored for applications in modern power grids*. Energies, 2017. **10**, DOI: 10.3390/en10122107.
37. G Zampardi and F La Mantia, Open challenges and good experimental practices in the research field of aqueous Zn-ion batteries. *Nature Communications*, 2022. **13**(1): p. 687.
38. LE Blanc, D Kundu, and LF Nazar, Scientific challenges for the implementation of Zn-ion batteries. *Joule*, 2020. **4**(4): p. 771-799.
39. C Li, S Jin, LA Archer, and LF Nazar, Toward practical aqueous zinc-ion batteries for electrochemical energy storage. *Joule*, 2022. **6**(8): p. 1733-1738.
40. PF Luckham and S Rossi, The colloidal and rheological properties of bentonite suspensions. *Advances in Colloid and Interface Science*, 1999. **82**(1): p. 43-92.
41. SB Hendricks and ME Jefferson, Structures of kaolin and talc-pyrophyllite hydrates and their bearing on water sorption of the clays. *American Mineralogist*, 1938. **23**(12): p. 863-875.
42. DE Smith, Molecular computer simulations of the swelling properties and interlayer structure of cesium montmorillonite. *Langmuir*, 1998. **14**(20): p. 5959-5967.
43. SM Pradhan, KS Katti, and DR Katti, Evolution of molecular interactions in the interlayer of Na-montmorillonite swelling clay with increasing hydration. *International Journal of Geomechanics*, 2015. **15**(5): p. 04014073.
44. M Garside. *Production volume of bentonite worldwide in 2020, by country*. 2022; Available from: https://www.statista.com/statistics/1312558/bentonite-production-volume-worldwide-by-country/.
45. M Garside. *Average bentonite price in the United States from 2010 to 2021*. 2022; Available from: https://www.statista.com/statistics/248186/average-bentonite-price/.
46. F Wang, O Borodin, T Gao, X Fan, W Sun, F Han, A Faraone, JA Dura, K Xu, and C Wang, Highly reversible zinc metal anode for aqueous batteries. *Nature Materials*, 2018. **17**(6): p. 543-549.
47. KY Choo and K Bai, Effects of bentonite concentration and solution pH on the rheological properties and long-term stabilities of bentonite suspensions. *Applied Clay Science*, 2015. **108**: p. 182-190.
48. M Wu, Y Zhang, L Xu, C Yang, M Hong, M Cui, BC Clifford, S He, S Jing, Y Yao, and L Hu, A sustainable chitosan-zinc electrolyte for high-rate zinc-metal batteries. *Matter*, 2022. **5**(10): p. 3402-3416.

49. B A. Salah, M S. Gaber, and AH T. Kandil, The removal of uranium and thorium from their aqueous solutions by 8-hydroxyquinoline immobilized bentonite. *Minerals*, 2019. **9**(10): p. 626.
50. H Komine, Theoretical equations on hydraulic conductivities of bentonite-based buffer and backfill for underground disposal of radioactive wastes. *Journal of Geotechnical and Geoenvironmental Engineering*, 2008. **134**(4): p. 497-508.
51. S Suzuki, S Prayongphan, Y Ichikawa, and B-G Chae, In situ observations of the swelling of bentonite aggregates in NaCl solution. *Applied Clay Science*, 2005. **29**(2): p. 89-98.
52. DM Anderson and PF Low, Density of water adsorbed on Wyoming bentonite. *Nature*, 1957. **180**(4596): p. 1194-1194.
53. F Kraehenbuehl, HF Stoeckli, F Brunner, G Kahr, and M Mueller-Vonmoos, Study of the water-bentonite system by vapour adsorption, immersion calorimetry and X-ray techniques: I. Micropore volumes and internal surface areas, following Dubinin's theory. *Clay Minerals*, 1987. **22**(1): p. 1-9.
54. G Montes-H, J Duplay, L Martinez, Y Geraud, and B Rousset-Tournier, Influence of interlayer cations on the water sorption and swelling–shrinkage of MX80 bentonite. *Applied Clay Science*, 2003. **23**(5): p. 309-321.
55. E Pomerantseva and Y Gogotsi, Two-dimensional heterostructures for energy storage. *Nature Energy*, 2017. **2**(7): p. 17089.
56. S Kaufhold, R Dohrmann, D Koch, and G Houben, The pH of aqueous bentonite suspensions. *Clays and Clay Minerals*, 2008. **56**(3): p. 338-343.
57. P Kumararaja, KM Manjaiah, SC Datta, TP Ahammed Shabeer, and B Sarkar, Chitosan-g-poly(acrylic acid)-bentonite composite: a potential immobilizing agent of heavy metals in soil. *Cellulose*, 2018. **25**(7): p. 3985-3999.
58. M Wang, A Emre, S Tung, A Gerber, D Wang, Y Huang, V Cecen, and NA Kotov, Biomimetic solid-state Zn^{2+} electrolyte for corrugated structural batteries. *ACS Nano*, 2019. **13**(2): p. 1107-1115.
59. C Liu, X Xie, B Lu, J Zhou, and S Liang, Electrolyte strategies toward better zinc-ion batteries. *ACS Energy Letters*, 2021. **6**(3): p. 1015-1033.
60. H van Olphen, Forces between suspended bentonite particles. *Clays and Clay Minerals*, 1955. **4**(1): p. 204-224.
61. Y Lv, Y Xiao, L Ma, C Zhi, and S Chen, Recent advances in electrolytes for “beyond aqueous” zinc-ion batteries. *Advanced Materials*, 2022. **34**(4): p. 2106409.
62. K Wu, J Huang, J Yi, X Liu, Y Liu, Y Wang, J Zhang, and Y Xia, Recent advances in polymer electrolytes for zinc ion batteries: Mechanisms, properties, and perspectives. *Advanced Energy Materials*, 2020. **10**(12): p. 1903977.
63. K Mizuno, Y Miyashita, Y Shindo, and H Ogawa, NMR and FT-IR studies of hydrogen bonds in ethanol-water mixtures. *The Journal of Physical Chemistry*, 1995. **99**(10): p. 3225-3228.
64. R Chua, Y Cai, PQ Lim, S Kumar, R Satish, W Manalastas, Jr., H Ren, V Verma, S Meng, SA Morris, P Kidkhunthod, J Bai, and M Srinivasan, Hydrogen-bonding interactions in hybrid aqueous/nonaqueous electrolytes enable low-cost and long-lifespan sodium-ion storage. *ACS Applied Materials & Interfaces*, 2020. **12**(20): p. 22862-22872.
65. P Jørgensen, Infrared study of water adsorbed on Wyoming bentonite. *Geologiska Föreningen i Stockholm Förhandlingar*, 1968. **90**(2): p. 213-220.

66. J Zhu, Z Bie, X Cai, Z Jiao, Z Wang, J Tao, W Song, and HJ Fan, A molecular-sieve electrolyte membrane enables separator-free zinc batteries with ultralong cycle life. *Advanced Materials*, 2022. **34**(43): p. 2207209.
67. Q Zhang, Y Ma, Y Lu, L Li, F Wan, K Zhang, and J Chen, Modulating electrolyte structure for ultralow temperature aqueous zinc batteries. *Nature Communications*, 2020. **11**(1): p. 4463.
68. K Ben Mabrouk, TH Kauffmann, H Aroui, and MD Fontana, Raman study of cation effect on sulfate vibration modes in solid state and in aqueous solutions. *Journal of Raman Spectroscopy*, 2013. **44**(11): p. 1603-1608.
69. ER Nightingale, Phenomenological theory of ion solvation. Effective radii of hydrated ions. *The Journal of Physical Chemistry*, 1959. **63**: p. 1381-1387.
70. C Huang, X Zhao, S Liu, Y Hao, Q Tang, A Hu, Z Liu, and X Chen, Stabilizing zinc anodes by regulating the electrical double layer with saccharin anions. *Advanced Materials*, 2021. **33**(38): p. 2100445.
71. Z Zhao, J Zhao, Z Hu, J Li, J Li, Y Zhang, C Wang, and G Cui, Long-life and deeply rechargeable aqueous Zn anodes enabled by a multifunctional brightener-inspired interphase. *Energy & Environmental Science*, 2019. **12**(6): p. 1938-1949.
72. P He, G Zhang, X Liao, M Yan, X Xu, Q An, J Liu, and L Mai, Sodium ion stabilized vanadium oxide nanowire cathode for high-performance zinc-ion batteries. *Advanced Energy Materials*, 2018. **8**(10): p. 1702463.
73. B Yong, D Ma, Y Wang, H Mi, C He, and P Zhang, Understanding the design principles of advanced aqueous zinc-ion battery cathodes: From transport kinetics to structural engineering, and future perspectives. *Advanced Energy Materials*, 2020. **10**(45): p. 2002354.
74. R Trócoli, A Morata, C Erinmwingbovo, F La Mantia, and A Tarancón, Self-discharge in Li-ion aqueous batteries: A case study on $LiMn_2O_4$. *Electrochimica Acta*, 2021. **373**: p. 137847.
75. L Suo, F Han, X Fan, H Liu, K Xu, and C Wang, "Water-in-Salt" electrolytes enable green and safe Li-ion batteries for large scale electric energy storage applications. *Journal of Materials Chemistry A*, 2016. **4**(17): p. 6639-6644.